Experimental observation of local rearrangements in dense quasi-two-dimensional emulsion flow

Dandan Chen,[1,2,*] Kenneth W. Desmond,[3,†] and Eric R. Weeks[3,‡]

[1]*School of Radiation Medicine and Protection, Medical College of Soochow University, Suzhou, China*

[2]*Collaborative Innovation Center of Radiation Medicine of Jiangsu Higher Education Institutions, Suzhou, China*

[3]*Department of Physics, Emory University, Atlanta, Georgia 30322, USA*

(Received 27 July 2014; revised manuscript received 30 April 2015; published 22 June 2015)

We experimentally study rearranging regions in slow athermal flow by observing the flow of a concentrated oil-in-water emulsion in a thin chamber with a constricting hopper shape. The gap of the chamber is smaller than the droplet diameters, so that the droplets are compressed into quasi-two-dimensional pancakes. We focus on localized rearrangements known as "T1 events" where four droplets exchange neighbors. Flowing droplets are deformed due to forces from neighboring droplets, and these deformations are decreased by nearby T1 events, with a spatial dependence related to the local structure. We see a tendency of the T1 events to occur in small clusters.

DOI: 10.1103/PhysRevE.91.062306 PACS number(s): 82.70.Kj, 83.80.Iz, 47.50.Gj

I. INTRODUCTION

A variety of soft materials can form dense jammed states, such as sand, foams, pastes, and emulsions [1–3]. Jammed materials behave like elastic solids for low applied stresses but flow like a liquid when the applied stress is above the yield stress [3–6]. If instead a constant strain is imposed, the stress can fluctuate macroscopically, and microscopically one observes complex rearrangements of the internal structure [4,5,7–10]. The macroscopic stress fluctuations likely arise from the fragile stress network where only a small subset of particles support most of the load [4,11–13]. An understanding of the plasticity of soft materials is based on the concept of localized plastic events first introduced by Argon [14]. These localized plastic events are responsible for the macroscopic fluctuations in the flow, with larger fluctuations associated with larger numbers of plastic events [6,15–19]. Simulations [7,10,20,21] and theoretical work [6,15–17,22–24] have connected local plastic rearrangements and the macroscopic flow. Experiments studying a variety of materials also provided details about local rearrangements and the length scale of their effects [9,25–28]. Studies of microscopic fluctuations have focused on dynamical heterogeneity, where at any given moment a subset of particles rearrange. Several experiments have examined dynamical heterogeneity in sheared colloidal glasses and granular materials [25–27,29–32].

A key control parameter for many soft materials is the volume fraction ϕ, the amount of sample occupied by the particles (in a granular material or colloidal suspension), droplets (in an emulsion), or bubbles (in a foam). Jamming occurs when ϕ exceeds a critical value ϕ_J, and it is for $\phi \geqslant \phi_J$ that these samples have a yield stress. Studies of hard (incompressible) particles are limited to $\phi \leqslant \phi_J$. Emulsions and foams are useful to study as they can be concentrated to $\phi \to 1$, due to the softness of droplets and bubbles. The rheology of three-dimensional emulsion samples has been studied [5,33,34], but the details of internal rearrangements were not measured. One recent study used confocal microscopy to study droplets in a sheared emulsion but did not study plastic flow [35]. Two-dimensional (2D) model systems are often used for probing flow properties on microscopic and mesoscopic length scales simultaneously [8,13,19,36–38]. Dry foams in 2D ($\phi = 1$) [18,39–41] are quite useful where elastic stresses can be determined from the polygonal shapes of bubbles, but those analysis techniques cannot be extended to wetter foams or emulsions ($\phi < 1$). In contrast, soft granular particles are useful for measuring forces and positions simultaneously [30,36] but are limited to lower area fractions close to jamming ($\phi \approx \phi_J$) due to the moderate stiffness of the particles.

In this paper we analyze experimental data from a quasi-two-dimensional (quasi-2D) flowing emulsion. In our experiment, small oil droplets are compressed into disks between two parallel glass plates. Before the flow is imposed, our samples are jammed with $\phi \approx 0.9 > \phi_J \approx 0.84$. These samples require a finite nonzero stress in order to flow. For each droplet, we measure the deviation of its outline from a circle and term this the deformation; these deviations are due to forces on the droplet from the surrounding droplets. We simultaneously measure macroscopic flow profiles, macroscopic and microscopic deformation, and the microscopic plastic events. The local plastic event we study is a "T1 event," a topological change of four droplets exchanging neighbors, indicated in Fig. 1 [3,8,19,20,41–43]. These are induced as the emulsion flows through a constricting hopper shape, shown in Fig. 2. The flow rate is controlled, and we observe evidence of large deformation fluctuations connected to the T1 events. We investigate the spatiotemporal change of droplet deformations around T1 events and show that the spatial structure of deformation relaxation is related to the local structure.

II. EXPERIMENTAL DETAILS

A. Flow chamber

For this paper, we use data from our previous experimental work [37] to study the spatial distribution of rearrangements in a flowing 2D emulsion. The experimental details are given in Ref. [37] but we reprise the key points here. Figure 2

*chendandan@suda.edu.cn

†Present address: ExxonMobil, Annandale, NJ 08801, USA.

‡erweeks@emory.edu

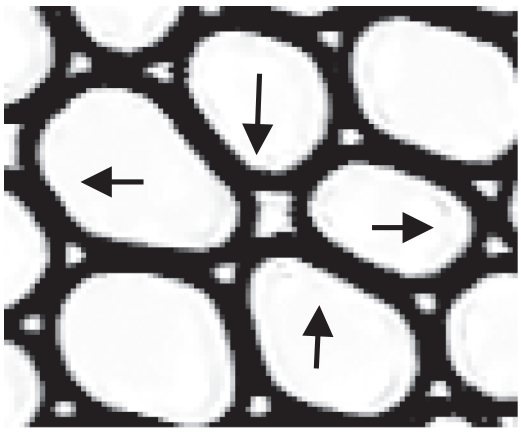

FIG. 1. A typical case of a T1 event: two droplets move apart and are no longer neighbors, and the other two come together to become neighbors. The field of view is 1.76×1.44 mm^2.

is a sketch of our experimental setup. The sample chamber has a gap of 0.10 ± 0.02 mm, controlled by a thin film of double-sided adhesive tape sandwiched between two glass plates. The droplets are silicone oil (poly-dimethylsiloxane, $\rho = 1$ g/mL, $\eta = 350$ mPa $\cdot$ s) in water, made by the "co-flow" microfluidic technique [44]. The droplets are stabilized by Fairy^{TM} soap with mass fraction 0.025. The adhesive tape is cut into a constricting hopper shape. A constant flux rate is set by a syringe pump attached to the left edge of the chamber. More details for our experimental runs are given in Table I.

The droplets have a diameter at least twice as large as the gap thickness, so that the droplets are compressed into pancake shapes, as indicated in Fig. 2(a). At a low area fraction, these droplets are circular in shape when viewed from below. For our experiments, the samples have area fraction $\phi \geqslant 0.90$, at which the samples are jammed (the jamming point is $\phi_J \approx 0.84$ for

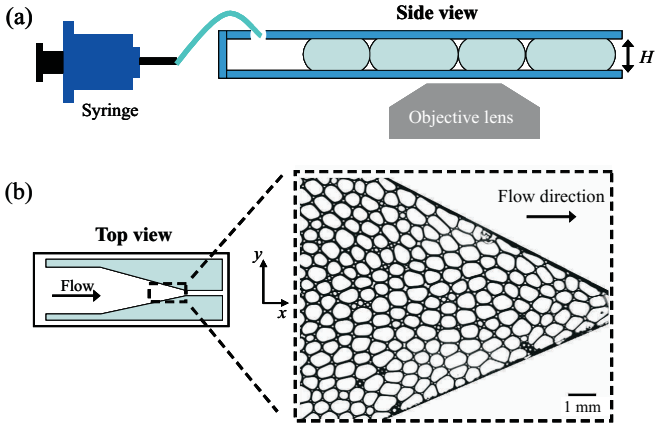

FIG. 2. (Color online) A sketch of the experimental setup. (a) Side view: oil droplets are compressed into disks between parallel glass plates and are driven by a syringe pump. (b) Top view: the spacers are cut into a contracting shape. The microscope field of view is indicated. The right is an experimental image, 11.2×8.5 mm^2, and flow direction is to the right. Note that at the left side of the image, the parallel edges are due to the limited field of view; the walls are still diagonal in this region.

TABLE I. Sample details of our six runs listed in seven columns: flux rate A (mm^2/s), normalized flux rate $\tilde{A} = A/\pi\langle r\rangle^2$ (s^{-1}), area fraction ϕ, droplet mean size $\langle r\rangle$ (mm), standard deviation $\sigma = \sqrt{\langle (r - \langle r\rangle)^2\rangle}$ normalized by $\langle r\rangle$, skewness $s = \langle (\frac{r-\langle r\rangle}{\sigma})^3\rangle$, and hopper angle Θ (degrees).

Data	A	$\tilde{A}$	ϕ	$\langle r\rangle$	$\sigma/\langle r\rangle$	s	Θ
1	2.93	12.8	0.90	0.27	0.21	0.01	25
2	1.33	18.8	0.90	0.15	0.17	−0.009	25
3	0.83	5.5	0.92	0.22	0.27	−0.010	27
4	0.75	14.1	0.93	0.13	0.24	−0.007	27
5	0.61	9.9	0.91	0.14	0.21	−0.010	26
6	0.33	6.2	0.94	0.13	0.28	−0.002	27

our samples) [45]. Because of this, the droplets press against one another, deforming their shapes as viewed from below and no longer appearing circular. In our image analysis techniques described below, it is this deformation (caused by neighboring droplets) that we analyze, as distinct from the deformation caused by the glass plates.

B. Image analysis

We use a bright-field microscope coupled to a CCD camera to record movies of our flowing emulsions at 30 frames per second. We collect our movies well into the contracting portion of the chamber, as indicated in Fig. 2(b). Due to the mismatch of the indices of refraction of oil and water, the droplet outlines are easy to see. From these outlines we identify the center of mass of each droplet area and also the perimeters of each droplet [38]. A small number of droplets rupture before they enter the flow chamber, and some of these tiny droplets are visible in Fig. 2(b). As these droplets always fit into the interstices of the larger droplets, we do not observe these tiny droplets playing any role in the experiment, but rather move passively. Accordingly, we discard these droplets ($r < 0.03$ mm) from our analysis; we do not track their motion.

To quantify the deformation of each droplet, we discretize the perimeter at 200 evenly spaced angles θ [see inset of Fig. 3(a)]. We quantify the deformation of droplets as the standard deviation of the radius $r(\theta)$:

$$D = \sqrt{\langle r^2\rangle - \langle r\rangle^2}/\langle r\rangle. \quad (1)$$

The values of D are shown in Fig. 3(a). Given the sample is at an area fraction above jamming, all droplets are compressed by their neighbors and thus are deformed so that $D > 0$. We have examined values of D for isolated droplets in other data sets, and note that pixelation results in $D \approx 0.03$ in these cases. This can be regarded as the uncertainty in D, although for this paper we only consider results where D is averaged over hundreds of droplets.

For our area fractions ($\phi \approx 0.9$), we observe that the mean value of the deformation in a quiescent sample is $D_0 = 0.06$. In flowing samples, droplets exert stronger forces on one another. These contact forces then deform the droplets further from round. In general, larger contact forces between a pair of droplets correspond with a longer contact length between the two droplets [38,46]. In turn, the contact length is related to the deformation, as demonstrated in Fig. 3(b). One limiting case

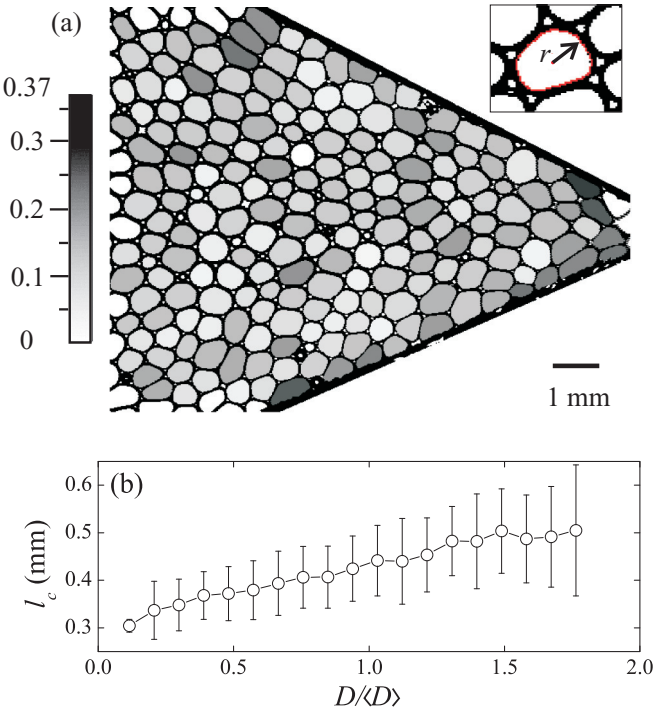

FIG. 3. (Color online) (a) The distribution of droplets shaded by the magnitude of deformation D, with the gray scale indicating the relative D values. Inset: sketch of r measured from the center of the droplet, used to define deformation in Eq. (1). (b) The mean value of the largest contact length on a droplet l_c as a function of its deformation D, normalized by the average $\langle D\rangle$. The correlation coefficient between the raw data (l_c and D) is ≈0.5. The error bars indicate the standard deviation of the data.

is when a droplet is surrounded by six neighboring droplets, all of which exert strong forces on the central droplet, and then the central droplet is deformed into a hexagonal shape with $D = 0.043$. This is a relatively small value of D, and for that matter, pixelation of the image would likely increase D above this value in our experiment. In contrast, a droplet feeling strong forces from only two adjacent droplets on opposite sides would be deformed into an oblong droplet with D able to grow arbitrarily large. Large D droplets, in other words, are those feeling large forces from two or three of their neighbors. These are often droplets participating in force chains [38]. This is qualitatively confirmed by observations of droplets with large D, such as shown in Fig. 3(a), where the darkest droplets (largest D) are oblong in shape. We cannot measure the exact forces in these experiments as the data were acquired with resolution inadequate to resolve forces (in order to achieve a larger field of view). At these slow flow rates and with the relatively large area fraction ($\phi \geqslant 0.90$), all viscous forces are an order of magnitude smaller than the repulsive droplet-droplet contact forces [38,47], so in large part values of D arise due to contacts with other droplets rather than viscous effects. However, note that immediately after a T1 event, the droplets feel strong contact forces moving them into their new positions within 2–4 s, and the relaxation of these forces is limited by viscosity (perhaps both bulk viscosity and interfacial viscosity [48]). This will be discussed more below.

We use standard particle-tracking routines [49,50] to track our droplets. These routines work best when droplet displacements between consecutive images are significantly less than the interdroplet distances, which is the case for our camera rate and flow rates.

We wish to study T1 events (Fig. 1). To identify a T1 event, we first identify the nearest neighbors of each droplet. As our samples are polydisperse, we use the Laguerre (radical) tessellation [51,52] to determine the nearest neighbors. Similar to the Voronoi tessellation, the Laguerre tessellation also partitions space into polygons, but uses the radius of each droplet as a weighting so that bigger droplets have polygons with larger areas. Droplets whose polygons share an edge are considered nearest neighbors. T1 events are cases where two droplets that are not neighbors converge and become nearest neighbors, and an adjacent two droplets diverge. Neighbor relations defined by tessellation algorithms are sensitive to positional noise, so to overcome this sensitivity, we further require that the separations must change by at least 5% in a time interval of 1 s. The time of the T1 event is when the topological neighbor change occurs.

III. FLOW PROFILES

At any given moment, the velocity field in our experiment fluctuates as droplets slide past the walls and one another. However, the time-averaged flow is straightforward to describe [37]. An example of the time-averaged velocity profile at a fixed x location is shown in Fig. 4(a). This velocity profile

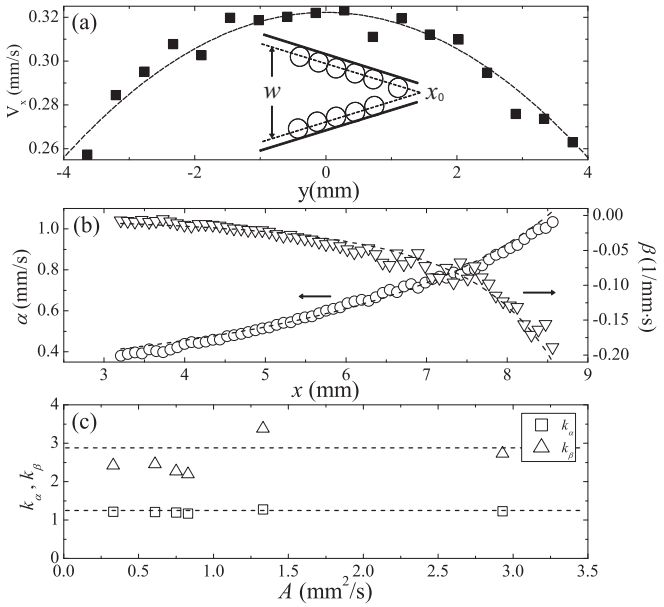

FIG. 4. (a) An example of the time-averaged velocity profile. The data are from Run 1, at a location where the channel width is $w \approx 8$ mm. The fit curve is Eq. (2). Inset: the width $w(x)$ is the range that droplet centers can reach, which is $\langle r\rangle$ away from the physical walls. (b) The parameters $\alpha(x)$ (circles) and $\beta(x)$ (triangles) obtained from fitting the flow profile with Eq. (2). Here the fit curves are from Eq. (3) with $k_\alpha = 1.23$ and $k_\beta = 2.73$. (c) k_α and k_β for all the six runs versus different flux rates. The dashed lines indicate the mean values $k_\alpha = 1.24$ and $k_\beta = 2.87$.

is parabolic, but does not go to zero at the edges of the flow chamber as droplets slip along the wall. The velocity profile is well described by

$$V_x(x,y) = \beta(x)y^2 + \alpha(x), \tag{2}$$

where $y = 0$ is the channel centerline, α is the flow rate along the centerline, and β relates to the local strain rate. $x = 0$ has no special meaning, although the inset to Fig. 4(a) identifies the useful location x_0 where the side walls would be separated by $2\langle r\rangle$.

The x-dependence of the parameters α and β is shown in Fig. 4(b), and their changes reflect the increasing flow speed as the channel narrows. The narrowing width of the channel is given by $w(x) = 2\tan(\Theta)(x_0 - x)$, the width of the channel that droplet centers can reach, as indicated in the inset sketch of Fig. 4(a). x_0 is where the walls are separated by $2\langle r\rangle$, that is, where the typical droplet would touch both walls without deforming. Thus, at the sample chamber walls, the droplets slide along the wall with velocity $V_x(x, \frac{w(x)}{2})$. Using $w(x)$, the parameters α and β are proportional to the flux rate A as

$$\alpha(x) = \frac{k_\alpha A}{w(x) + 2\langle r\rangle}, \quad \beta(x) = \frac{-k_\beta A}{w^3(x) + 6\langle r\rangle w^2(x)}, \tag{3}$$

as shown by the fit lines in Fig. 4(b). The fit parameters k_α and k_β appear fairly independent of the flux rate in our experimental runs [Fig. 4(c)]. Overall, the functional forms of Eqs. (3) and the values of the fit parameters are consistent with a constant (x-independent) flux, as required. In particular, $k_\alpha - k_\beta/12 = 1$ is required for constant flux [37], and this is satisfied by our fit values (given in the Fig. 4 caption). These results apply for the oil droplets only, and assume that the water flows at the same rate as the droplets, which is not a perfect assumption [53,54]. Given the high area fractions of our experiment, and the fact that the observed area fraction does not change during the experiment, the assumption of constant flux seems adequate.

$V_y(x,y)$ can be worked out from the condition that $\vec{\nabla}\cdot\vec{V} = 0$ (as our flow is incompressible). Using the approximation $w \gg \langle r\rangle$, it can be shown that

$$V_y(x,y) \approx -\frac{y}{w(x)}(2\tan\Theta)V_x(x,y). \tag{4}$$

$2\tan\Theta \approx 1$ for our hopper angles Θ, and the maximum value for $|y|$ is $w(x)/2$, so V_y is no more than half the value of V_x.

Note that several prior experiments found that the velocity profile of a foam is strongly influenced by the glass plates confining the sample (the plates making the sample quasi-2D) [55,56]. Those experiments used shear imposed at the side boundaries and found that the sample motion was localized near the moving boundary. However, when the experiments were repeated without a confining glass wall (using a bubble raft floating on a water surface), there was no shear localization. With our flow geometry, the forcing is due to a pump rather than motion of side walls, and we do not observe shear localization. Nonetheless, the velocity profile might be different for flows with the same geometry as our experiments, but without confining glass plates.

In the absence of flow, droplets would all have similar values for their deformation, $D_0 = 0.06$ for the area fraction $\phi \approx 0.9$ relevant for our data. With flow, we find the time-averaged deformation depends on the flux rate A and the x position as $\langle D\rangle_{y,t}(x) = D_0[1 + A/k_v w(x)]$, where $k_v = 0.81$ mm/s is a velocity scale. While this is an empirical result, we note that $A/w(x)$ is proportional to the mean flow speed $\langle V_x\rangle_y$ at a given x. This is sensible, as the increase of $\langle D\rangle_y$ over D_0 is due to the fact that droplets deform when they rearrange, and then viscous forces slows the relaxation of the droplet deformations back to their equilibrium level. In most of our analysis below, we focus on the left side of the sample chamber where $w(x)$ is large [where the walls are no longer visible, see Fig. 3(a)]. In this region, the average deformation $\langle D\rangle_{y,t}$ varies with x by at most 20% (for the largest A) and more typically 10% or less. The mean shear rate in this region is $\bar{\dot{\gamma}} \sim 0.01\ \mathrm{s}^{-1}$ and is in the range used in a number of previous experiments [8,20,55,57].

The dependence of deformation on flux rate shows that our experiment is not in a rate-independent regime. Furthermore, a prior experimental study of a sheared bubble raft provides strong evidence that even slow steady flow is not equivalent to the quasistatic limit [57]. Nonetheless, all relevant time scales appear to be set by the flow rate for our data. This will be discussed where relevant (as above for the velocity profiles, and in Sec. IV A for the rates of T1 events). Furthermore, all our results below are normalized by the average deformation for each experiment, to remove the flow rate dependence of D.

IV. DEFORMATION FLUCTUATIONS AND T1 EVENTS

A. Spatial averages

Although the macroscopic time-averaged velocity field is well defined, the microscopic flow has strong temporal fluctuations. To quantify this, we study the properties of the droplets at the left side of the image, in the region where we do not see the hopper walls [see Fig. 3(a)]. This region contains ~100 droplets, and we average their deformations at every time. We then apply a running-time average using a window of 0.33 s (to reduce the noise), and then divide the time series by its time-averaged value, terming this result $D_G(t)$, the global deformation. Due to the normalization $\langle D_G(t)\rangle_t \equiv 1$. Similar to previous granular [21,58,59] and foam [8,18,57,60–62] experiments, large deformation fluctuations are observed in Fig. 5. The power spectrum (inset) shows a tendency of power-law decay $P(\omega) \sim \omega^{-1}$ at high frequencies, comparable to spectra found in granular flows [21,58,59].

To quantify the deformation releases, we define deformation changes ΔD_G between local extrema of $D_G(t)$. For example, the inset of Fig. 5 shows an example where $\Delta D_G < 0$. The time interval between subsequent local extrema is τ. Figure 6(a) shows a scatter plot of the relation between ΔD_G and τ. In general, larger changes of D_G take longer times. The different colors indicate different flow rates A and no dependence on the flow rate is seen. The time scale τ is primarily set by viscosity, and given that all of our samples have similar area fractions this time scale should be relatively constant (1–3 s), depending mainly on the number of T1 events relaxing [47].

The probability distribution of event sizes ΔD_G is shown in Fig. 6(b). Large events are rare, but not as rare as would be predicted from the Gaussian fit (dashed line) shown in the plot. Our distribution is slightly broader than a previous foam experiment, which found a Gaussian distribution for a

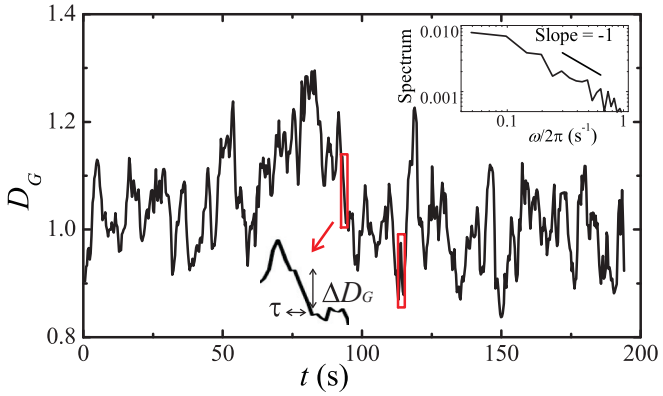

FIG. 5. (Color online) Temporal fluctuations of the global deformation D_G from Run 1. The data are smoothed by a time window of 0.33 s to reduce noise. The red time windows indicate two events ($93.9 < t < 95.6$ s and $115.0 < t < 116.4$ s), corresponding to the T1 events shown in Fig. 8(a). The top-right inset is the power spectrum of the data, with the line showing the power law $P(\omega) \sim \omega^{-1}$. The bottom inset shows the definitions of ΔD_G and τ.

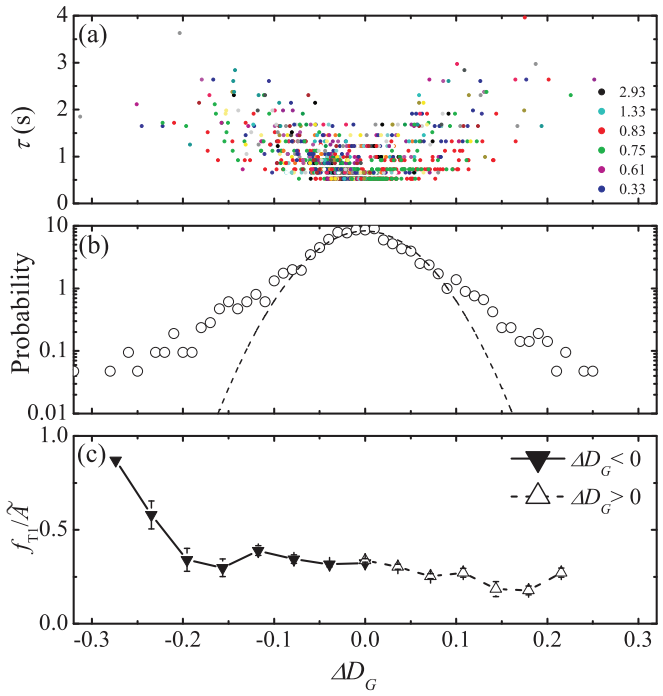

FIG. 6. (Color) (a) Scatter plot of the time τ between local extrema of $D_G(t)$, as a function of the change ΔD_G between the extrema; see the lower inset of Fig. 5 for definitions of these two variables. The horizontal bands are due to our limited time resolution. The colors indicate the flux rate $\tilde{A}$ in units of mm^2/s. (b) Probability distribution function of ΔD_G. The dashed line is a Gaussian fit with width 0.044. (c) The T1 frequency f_{T1} normalized by the flux rate $\tilde{A} = A/\pi\langle r\rangle^2$, plotted as as a function of the size of the deformation change. The error bars are the standard error of the mean. For the point at far left, there is only one observation with this magnitude of ΔD_G, so no error bar is shown. For panels (b) and (c) the six experimental runs are averaged together.

similar quantity [18], perhaps because the flow geometry was quite different. In our data, there is a slightly larger probability for large decreases of D_G as compared to increases. Here, data for different flow rates $\tilde{A}$ are averaged together, but the individual distributions look similar. In particular, they have similar widths: width $=0.048 \pm 0.009$ for the six experiments, with the uncertainty being the standard deviation, as compared to the width for the aggregated data of 0.044. No systematic dependence on $\tilde{A}$ is seen in the widths from the individual experiments. This is, of course, as long as the data being compared are the normalized D_G rather than the raw D; otherwise, the slight dependence of $\langle D\rangle$ on $\tilde{A}$ is seen in the larger widths for larger $\tilde{A}$.

A connection between large deformation drops and T1 events has been observed before in foams [18,62], as well as in our prior analysis of these emulsion experiments [37]. For illustration, T1 events within the highlighted time windows of Fig. 5 are shown in Fig. 8(a). Here we quantify this connection in a different way that highlights that there is a "background" rate of T1 events, but that the largest decreases of the deformation are connected to a higher rate of T1 events [19]. We define the frequency of T1 events as the number of T1 events N_{T1} occurring in a given time interval τ [between extrema of $D_G(t)$], divided by τ, that is, $f_{T1} = N_{T1}/\tau$. There is a trivial dependence on $\tilde{A}$—faster flows have higher rates of T1 events—so accordingly we normalize the T1 frequency by considering the nondimensional quantity $f_{T1}/\tilde{A}$. In Fig. 6(c), we plot the T1 frequency as a function of the size of the deformation change ΔD_G for both decreases (solid triangles) and increases (open triangles). For small increases or decreases, the T1 frequency is fairly constant. For larger decreases of D_G ($\Delta D_G \lesssim -0.2$), the T1 frequency is markedly larger as well, although as Fig. 6(b) makes clear, this is based on a relatively small number of events. Similar to the discussion in the previous paragraph, here again if we analyze the data for each experiment separately, the data all show $f_{T1}/\tilde{A}$ decreasing for larger ΔD_G. For each individual experiment, the downward slope is similar to that seen from the combined data shown in Fig. 6(c), and again no systematic dependence on $\tilde{A}$ is seen.

B. Local spatial structure

Given the correlation between T1 events and global deformation relaxations, we next examine how a T1 event changes the local deformation field D of the nearby droplets. Figure 7(a) is the spatial-temporal map of the local deformation field around a T1 event. The lag time $\Delta t = 0$ is the instant of a T1 event, and the distance $\Delta R = 0$ is the center of the four droplets undergoing the T1 event in their comoving reference frame. The map color indicates the magnitude of the mean deformation D of individual droplets compared to the global mean $\langle D_G\rangle$ (white): $D < \langle D_G\rangle$ is indicated by blue, and $D > \langle D_G\rangle$ is indicated by red. When a T1 event happens, the local deformation first builds up (deep red $\sim 1.5\langle D_G\rangle$), and this drops dramatically after the T1 event, turning the color from deep red to deep blue. The blue region afterward splits into two parts due to the neighbor exchange: one locates around $\Delta R \leqslant \langle r\rangle$ corresponding to the converging pair, and another locates around $\Delta R = 2\langle r\rangle$ corresponding to the diverging pair.

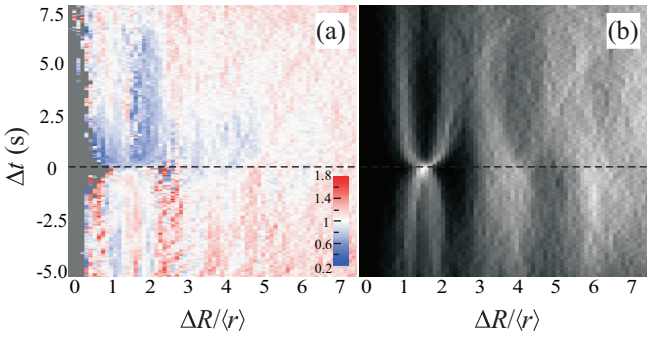

FIG. 7. (Color) (a) Spatial-temporal map of the local deformation values around a T1 event, averaged over 186 T1 events during a 194-s duration movie (Run 1). The distance ΔR is defined in the frame of reference comoving with the center of the four droplets undergoing T1 rearrangements, at a speed of roughly one mean radius per second. $\Delta t = 0$ is the moment when the T1 event occurs, indicated by the horizontal dashed line. The color indicates the mean magnitude of the deformation D on individual droplets compared to the global mean (white), where smaller values are blue and larger values are red, as indicated by the color bar. (b) The droplet number density is indicated by brightness. The bright spot at $\Delta R/\langle r\rangle = 1.5, \Delta t = 0$ corresponds to the four droplets undergoing the T1 event, as $\Delta t = 0$ is defined when they are all equidistant from the center of the event. Qualitatively similar images are seen for the different experiments; we show here Run 1, which has the most T1 events observed.

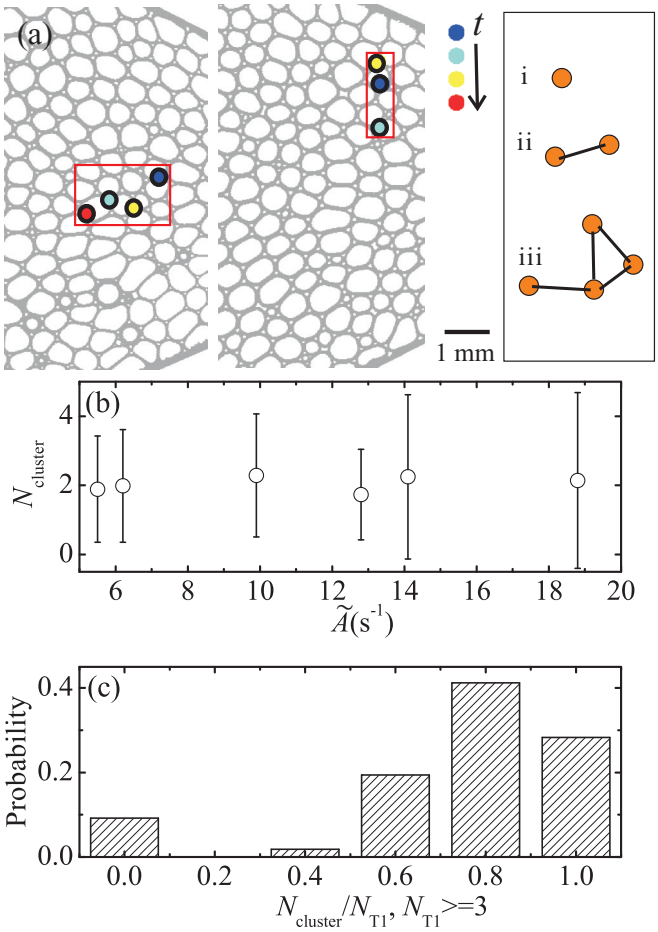

FIG. 8. (Color online) (a) Spatial distribution of consecutive T1 events during the large deformation drops corresponding to the time windows of Fig. 5. The colored circles show the positions of the T1 events (at the center of the four droplets) at $t = 94.1$, 94.5, 95.3, and 95.5 s and $t = 115.7$, 116.1, and 116.3 s for each event. The color ordering is dark blue (first) to red (last). The background images are taken at $t = 95$ s and $t = 116$ s. The sketch on the right shows an example of clusters of T1 events. Each point indicates the center of a T1 event, and so the number of T1 events is $N_{T1} = 7$ in this case. Black bonds indicate those with separations less than $6\langle r\rangle$. In this case, the seven T1 events are composed of three distinct clusters, and the largest cluster has $N_{\text{cluster}} = 4$. (b) The mean largest cluster size N_{cluster} as a function of the nondimensional flux rate $\tilde{A}$. The error bars indicate the standard deviation. (c) The probability distribution of ratio $N_{\text{cluster}}/N_{T1}$ for data with $N_{T1} \geqslant 3$.

The spatial structure is confirmed by the particle density map in the same frame of reference in Fig. 7(b), where white shades indicate more probable positions of droplets relative to the T1 event.

The relaxation is asymmetric among the two pairs of droplets in the T1 event. The length of the blue region along the time axis for the diverging pair is much longer than for the converging pair. This suggests the diverging droplets have their shape relaxed more significantly than the converging droplets. Furthermore, the blue region where the deformation decreases extends along the ΔR axis to a distance up to $5\langle r\rangle$. Note that we are only focusing on ΔR dependence and averaging over any angular dependence that might be present (angular dependence has been suggested by simulations [16]). Overall, viscous forces help determine the moderately short time over which the pattern changes in Fig. 7 after the T1 event. That is, in the absence of viscosity, the T1 event would be expected to snap the droplets into place instantaneously.

C. Clusters of T1 events

Given that T1 events affect nearby droplets (Fig. 7), one T1 event sometimes triggers other T1 events, forming a relaxing region with a larger length scale. Figure 8(a) shows small clusters of T1 events during two time windows of global deformation drops (Fig. 5). To quantify these rearranging regions during global deformation releases, we investigate clusters of neighboring T1 events with separations less than $6\langle r\rangle$. The choice of this separation cutoff is motivated by the distance where the deformation visibly relaxes in Fig. 7(a). To be considered part of the same T1 cluster, the T1 events are required to occur during an interval where $D_G(t)$ drops monotonically. Furthermore, we focus only on the largest T1 cluster in each global deformation release. As shown in Fig. 8(b), the sizes of those largest clusters N_{cluster} are fairly small (a mean value close to 2) and have no dependence on the flux rate in these experiments. Given the small sizes of these clusters, we checked to see if random chance could form clusters of similar sizes. To do this, we took the data of all cluster positions (x, y, t) and randomly shuffled the t values. This keeps constant the number of T1 events occurring at any time t but effectively randomizes their positions. The cluster sizes formed after this shuffling are smaller by 0.4 on average (that is, ≈1.6 particles rather than ≈2.0). Cluster sizes of the

values we see are found only 1% of the time in the shuffled data. This strongly suggests that our clusters, while quite small, nonetheless indicate some true spatial correlations between T1 events.

An alternate way to quantify the clustering is to consider the number N_{T1} of T1 events during a given global deformation release, and then compare this to the size of the largest cluster during that event N_{cluster}. If all T1 events are clustered together, then the ratio $N_{\text{cluster}}/N_{T1} = 1$. For small events with $N_{T1} = 2$, this ratio is $\approx$0.5 on average, indicating that these T1 events are often uncorrelated in space. For larger events with $N_{T1} \geqslant 3$, we plot the probability distribution of the ratio $N_{\text{cluster}}/N_{T1}$ in Fig. 8(c). The peak of the distribution is around 0.8, showing that these larger bursts of T1 events often cluster spatially.

V. CONCLUSIONS

We have studied the link between local rearrangement events (T1 events) and global deformation relaxations in a 2D emulsion experiment. We see that the droplets deform during the flow as they are compressed by other droplets. The flow is steady, but the global mean deformation has large temporal fluctuations. Large decreases of the global deformation are correlated with small cascades of local T1 events in agreement with previous studies of 2D foams [60,62]. We also find that T1 events decrease the deformation of nearby droplets, with a spatial pattern related to the local spatial structure of the droplets. Noticeable decreases of the deformation are seen as far as three diameters away, suggestive of the "flow cooperativity length" predicted by theory [6,15] and suggested by previous experiments [6,62–65] and simulations [10]. We find T1 events tend to form small clusters, especially in cases where the global deformation decreases the most. To an extent, some characteristics of flowing dense amorphous materials are independent of their microscopic details [17,66–68], and so our results may be relevant for flow of three-dimensional amorphous materials, although of course the definition of rearrangements will be different [9,34]. Overall, we confirm a connection between cascades of local rearrangements and macroscopic fluctuations of the sample behavior, with the latter quantified by the instantaneous mean global deformation of the flowing droplets.

ACKNOWLEDGMENTS

We thank S. Devaiah, A. Fernandez-Nieves, S. Hilgenfeldt, X. Hong, S. Vivek, and P. J. Young for helpful discussions. This work was supported by the National Science Foundation under Grants No. CBET-0853837 and No. CBET-1336401. D.C. was supported by the National Natural Science Foundation of China (Grant No. 11304212) and the Natural Science Foundation of Jiangsu Province of China (Grant No. BK20130279).

[1] A. J. Liu and S. R. Nagel, Nonlinear dynamics: Jamming is not just cool anymore, Nature **396**, 21 (1998).
[2] D. T. N. Chen, Q. Wen, P. A. Janmey, J. C. Crocker, and A. G. Yodh, Rheology of soft materials, Ann. Rev. Cond. Mat. Phys. **1**, 301 (2010).
[3] B. Dollet and C. Raufaste, Rheology of aqueous foams, C. R. Phys. **15**, 731 (2014).
[4] M. E. Cates, J. P. Wittmer, J.-P. Bouchaud, and P. Claudin, Jamming, force chains, and fragile matter, Phys. Rev. Lett. **81**, 1841 (1998).
[5] P. Coussot, J. S. Raynaud, F. Bertrand, P. Moucheront, J. P. Guilbaud, H. T. Huynh, S. Jarny, and D. Lesueur, Coexistence of liquid and solid phases in flowing soft-glassy materials, Phys. Rev. Lett. **88**, 218301 (2002).
[6] J. Goyon, A. Colin, G. Ovarlez, A. Ajdari, and L. Bocquet, Spatial cooperativity in soft glassy flows, Nature **454**, 84 (2008).
[7] D. J. Durian, Foam mechanics at the bubble scale, Phys. Rev. Lett. **75**, 4780 (1995).
[8] J. Lauridsen, G. Chanan, and M. Dennin, Velocity profiles in slowly sheared bubble rafts, Phys. Rev. Lett. **93**, 018303 (2004).
[9] A. Amon, V. B. Nguyen, A. Bruand, J. Crassous, and E. Clément, Hot spots in an athermal system, Phys. Rev. Lett. **108**, 135502 (2012).
[10] V. Mansard, A. Colin, P. Chaudhuri, and L. Bocquet, A molecular dynamics study of non-local effects in the flow of soft jammed particles, Soft Matter **9**, 7489 (2013).
[11] J. Brujic, S. Fedwards, I. Hopkinson, and H. Makse, Measuring the distribution of interdroplet forces in a compressed emulsion system, Physica A **327**, 201 (2003).
[12] J. Zhou, S. Long, Q. Wang, and A. D. Dinsmore, Measurement of forces inside a three-dimensional pile of frictionless droplets, Science **312**, 1631 (2006).
[13] L. Zhang, S. Cai, Z. Hu, and J. Zhang, A comparison between bridges and force-chains in photoelastic disk packing, Soft Matter **10**, 109 (2014).
[14] A. S. Argon, Plastic deformation in metallic glasses, Acta Metall. **27**, 47 (1979).
[15] L. Bocquet, A. Colin, and A. Ajdari, Kinetic theory of plastic flow in soft glassy materials, Phys. Rev. Lett. **103**, 036001 (2009).
[16] G. Picard, A. Ajdari, F. Lequeux, and L. Bocquet, Elastic consequences of a single plastic event: A step towards the microscopic modeling of the flow of yield stress fluids, Eur. Phys. J. E **15**, 371 (2004).
[17] K. Kamrin and G. Koval, Nonlocal constitutive relation for steady granular flow, Phys. Rev. Lett. **108**, 178301 (2012).
[18] B. Dollet and F. Graner, Two-dimensional flow of foam around a circular obstacle: Local measurements of elasticity, plasticity and flow, J. Fluid Mech. **585**, 181 (2007).
[19] P. Marmottant, C. Raufaste, and F. Graner, Discrete rearranging disordered patterns, part II: 2D plasticity, elasticity and flow of a foam, Eur. Phys. J. E **25**, 371 (2008).
[20] A. Kabla and G. Debregeas, Local stress relaxation and shear banding in a dry foam under shear, Phys. Rev. Lett. **90**, 258303 (2003).
[21] S. Tewari, B. Tithi, A. Ferguson, and B. Chakraborty, Growing length scale in gravity-driven dense granular flow, Phys. Rev. E **79**, 011303 (2009).

[22] F. Spaepen, A microscopic mechanism for steady state inhomogeneous flow in metallic glasses, Acta Metall. **25**, 407 (1977).
[23] M. L. Falk and J. S. Langer, Dynamics of viscoplastic deformation in amorphous solids, Phys. Rev. E **57**, 7192 (1998).
[24] A. Nicolas and J. L. Barrat, Spatial cooperativity in microchannel flows of soft jammed materials: A mesoscopic approach, Phys. Rev. Lett. **110**, 138304 (2013).
[25] P. Schall, D. A. Weitz, and F. Spaepen, Structural rearrangements that govern flow in colloidal glasses, Science **318**, 1895 (2007).
[26] L. Isa, R. Besseling, A. N. Morozov, and W. C. K. Poon, Velocity oscillations in microfluidic flows of concentrated colloidal suspensions, Phys. Rev. Lett. **102**, 058302 (2009).
[27] D. Chen, D. Semwogerere, J. Sato, V. Breedveld, and E. R. Weeks, Microscopic structural relaxation in a sheared supercooled colloidal liquid, Phys. Rev. E **81**, 011403 (2010).
[28] K. Nichol and M. van Hecke, Flow-induced agitations create a granular fluid: Effective viscosity and fluctuations, Phys. Rev. E **85**, 061309 (2012).
[29] R. Besseling, L. Isa, E. R. Weeks, and W. C. K. Poon, Quantitative imaging of colloidal flows, Adv. Colloid Interface Sci. **146**, 1 (2009).
[30] B. Utter and R. P. Behringer, Experimental measures of affine and nonaffine deformation in granular shear, Phys. Rev. Lett. **100**, 208302 (2008).
[31] E. Wandersman, J. A. Dijksman, and M. van Hecke, Particle diffusion in slow granular bulk flows, Europhys. Lett. **100**, 38006 (2012).
[32] K. E. Jensen, D. A. Weitz, and F. Spaepen, Local shear transformations in deformed and quiescent hard-sphere colloidal glasses, Phys. Rev. E **90**, 042305 (2014).
[33] P. Hébraud, F. Lequeux, J. P. Munch, and D. J. Pine, Yielding and rearrangements in disordered emulsions, Phys. Rev. Lett. **78**, 4657 (1997).
[34] P. Jop, V. Mansard, P. Chaudhuri, L. Bocquet, and A. Colin, Microscale rheology of a soft glassy material close to yielding, Phys. Rev. Lett. **108**, 148301 (2012).
[35] J. Clara-Rahola, T. A. Brzinski, D. Semwogerere, K. Feitosa, J. C. Crocker, J. Sato, V. Breedveld, and E. R. Weeks, Affine and nonaffine motions in sheared polydisperse emulsions, Phys. Rev. E **91**, 010301(R) (2015).
[36] R. R. Hartley and R. P. Behringer, Logarithmic rate dependence of force networks in sheared granular materials, Nature **421**, 928 (2003).
[37] D. Chen, K. W. Desmond, and E. R. Weeks, Topological rearrangements and stress fluctuations in quasi-two-dimensional hopper flow of emulsions, Soft Matter **8**, 10486 (2012).
[38] K. W. Desmond, P. J. Young, D. Chen, and E. R. Weeks, Experimental study of forces between quasi-two-dimensional emulsion droplets near jamming, Soft Matter **9**, 3424 (2013).
[39] M. Asipauskas, M. Aubouy, J. A. Glazier, F. A. Graner, and Y. Jiang, A texture tensor to quantify deformations: The example of two-dimensional flowing foams, Granular Matter **5**, 71 (2003).
[40] A. Kabla, J. Scheibert, and G. Debregeas, Quasi-static rheology of foams. Part 2. Continuous shear flow, J. Fluid Mech. **587**, 45 (2007).
[41] F. Graner, B. Dollet, C. Raufaste, and P. Marmottant, Discrete rearranging disordered patterns, part I: Robust statistical tools in two or three dimensions, Eur. Phys. J. E **25**, 349 (2008).
[42] S. Hilgenfeldt, S. Arif, and J.-C. Tsai, Foam: A multiphase system with many facets, Philos. Trans. R. Soc. London A **366**, 2145 (2008).
[43] D. Weaire, J. D. Barry, and S. Hutzler, The continuum theory of shear localization in two-dimensional foam, J. Phys. Condens. Matter **22**, 193101 (2010).
[44] R. Shah, H. Shum, A. Rowat, D. Lee, J. Agresti, A. Utada, L. Chu, J. Kim, A. Fernandez-Nieves, and C. Martinez, Designer emulsions using microfluidics, Mater. Today **11**, 18 (2008).
[45] N. Xu, J. Blawzdziewicz, and C. S. O'Hern, Random close packing revisited: Ways to pack frictionless disks, Phys. Rev. E **71**, 061306 (2005).
[46] O. Campas, T. Mammoto, S. Hasso, R. A. Sperling, D. O'Connell, A. G. Bischof, R. Maas, D. A. Weitz, L. Mahadevan, and D. E. Ingber, Quantifying cell-generated mechanical forces within living embryonic tissues, Nature Methods **11**, 183 (2014).
[47] K. W. Desmond, Structure, dynamics, and forces of jammed systems, Ph.D. thesis, Emory University, 2012.
[48] M. Durand and H. Stone, Relaxation time of the topological t1 process in a two-dimensional foam, Phys. Rev. Lett. **97**, 226101 (2006).
[49] J. C. Crocker and D. G. Grier, Methods of digital video microscopy for colloidal studies, J. Colloid Interface Sci. **179**, 298 (1996).
[50] E. R. Weeks and J. C. Crocker, Particle tracking using IDL, http://www.physics.emory.edu/∼weeks/idl/.
[51] H. Telley, T. M. Liebling, and A. Mocellin, The laguerre model of grain growth in two dimensions i. Cellular structures viewed as dynamical laguerre tessellations, Philos. Mag. B **73**, 395 (1996).
[52] B. Gellatly, Characterisation of models of multicomponent amorphous metals: The radical alternative to the voronoi polyhedron, J. Non-Cryst. Solids **50**, 313 (1982).
[53] F. Fairbrother and A. E. Stubbs, Studies in electro-endosmosis. Part VI. The "bubble-tube" method of measurement, J. Chem. Soc. 527 (1935).
[54] F. P. Bretherton, The motion of long bubbles in tubes, J. Fluid Mech. **10**, 166 (1961).
[55] Y. Wang, K. Krishan, and M. Dennin, Impact of boundaries on velocity profiles in bubble rafts, Phys. Rev. E **73**, 031401 (2006).
[56] G. Katgert, B. P. Tighe, M. E. Möbius, and M. van Hecke, Couette flow of two-dimensional foams, Europhys. Lett. **90**, 54002 (2010).
[57] M. Twardos and M. Dennin, Comparison between step strains and slow steady shear in a bubble raft, Phys. Rev. E **71**, 061401 (2005).
[58] E. Longhi, N. Easwar, and N. Menon, Large force fluctuations in a flowing granular medium, Phys. Rev. Lett. **89**, 045501 (2002).
[59] E. Gardel, E. Sitaridou, K. Facto, E. Keene, K. Hattam, N. Easwar, and N. Menon, Dynamical fluctuations in dense granular flows, Phil. Trans. R. Soc. A **367**, 5109 (2009).
[60] J. Lauridsen, M. Twardos, and M. Dennin, Shear-induced stress relaxation in a two-dimensional wet foam, Phys. Rev. Lett. **89**, 098303 (2002).
[61] E. Pratt and M. Dennin, Nonlinear stress and fluctuation dynamics of sheared disordered wet foam, Phys. Rev. E **67**, 051402 (2003).
[62] M. Dennin, Statistics of bubble rearrangements in a slowly sheared two-dimensional foam, Phys. Rev. E **70**, 041406 (2004).

[63] G. Katgert, A. Latka, M. E. Möbius, and M. van Hecke, Flow in linearly sheared two-dimensional foams: From bubble to bulk scale, Phys. Rev. E **79**, 066318 (2009).

[64] G. Katgert and M. van Hecke, Jamming and geometry of two-dimensional foams, Europhys. Lett. **92**, 34002 (2010).

[65] C. Gilbreth, S. Sullivan, and M. Dennin, Flow transitions in two-dimensional foams, Phys. Rev. E **74**, 051406 (2006).

[66] P. Sollich, F. Lequeux, P. Hébraud, and M. E. Cates, Rheology of soft glassy materials, Phys. Rev. Lett. **78**, 2020 (1997).

[67] G. D'Anna and G. Gremaud, The jamming route to the glass state in weakly perturbed granular media, Nature **413**, 407 (2001).

[68] R. Lespiat, S. C. Addad, and R. Höhler, Jamming and flow of random-close-packed spherical bubbles: An analogy with granular materials, Phys. Rev. Lett. **106**, 148302 (2011).